UC Berkeley
UC Berkeley Previously Published Works

Title
Temperature-driven growth of antiferromagnetic domains in thin-film FeRh

Permalink
https://escholarship.org/uc/item/4z07k9zv

Journal
Journal of Physics Condensed Matter, 27(25)

ISSN
0953-8984

Authors
Baldasseroni, C
Bordel, C
Antonakos, C
et al.

Publication Date
2015-06-23

DOI
10.1088/0953-8984/27/25/256001

Peer reviewed

Temperature-driven growth of antiferromagnetic domains in thin-film FeRh

C Baldasseroni[1]**, C Bordel**[2,3,4]**, C Antonakos**[5]**, A Scholl**[6]**, K H Stone**[4]**,**
J B Kortright[4] **and F Hellman**[3,4]

[1] Department of Materials Science and Engineering, University of California Berkeley, Berkeley,
CA 94720, USA
[2] GPM, UMR CNRS 6634, Université de Rouen, Av. de l'Université—BP12, 76801 St Etienne
du Rouvray, France
[3] Department of Physics, University of California Berkeley, Berkeley, CA 94720, USA
[4] Materials Sciences Division, Lawrence Berkeley National Laboratory, 1 Cyclotron Rd, Berkeley,
CA 94270, USA
[5] Department of Chemistry, University of California Berkeley, Berkeley, CA 94720, USA
[6] Advanced Light Source, Lawrence Berkeley National Laboratory, 1 Cyclotron Rd, Berkeley,
CA 94270, USA

E-mail: cbaldasseroni@berkeley.edu

CrossMark

Abstract

The evolution of the antiferromagnetic phase across the temperature-driven ferromagnetic (FM) to antiferromagnetic (AF) phase transition in epitaxial FeRh thin films was studied by x-ray magnetic linear and circular dichroism (XMLD and XMCD) and photoemission electron microscopy. By comparing XMLD and XMCD images recorded at the same temperature, the AF phase was identified, its structure directly imaged, and its evolution studied across the transition. A quantitative analysis of the correlation length of the images shows differences between the characteristic length scale of the two phases with the AF phase having a finer feature size. The asymmetry of the transition from FM to AF upon cooling and AF–FM upon heating is evidenced: upon cooling the formation of AF phase is dominated by nucleation at defects, with little subsequent growth, resulting in a small and non-random final AF domain structure, while upon heating, heterogeneous nucleation at different sites followed by significant domain size growth of the FM phase is observed, resulting in a non-reproducible final FM large domain structure.

Keywords: magnetic films, magnetic phase transitions, XMLD

(Some figures may appear in colour only in the online journal)

1. Introduction

Equiatomic FeRh was discovered in 1939 by Fallot *et al* to undergo an unusual temperature-driven magnetic phase transition [1] later identified as a first order antiferromagnetic (AF) to ferromagnetic (FM) transition with increasing temperature [2, 3]. The first order character of this phase transition was evidenced in the discontinuous and hysteretic change with temperature, field, and pressure of different properties such as magnetization [1–3], resistivity [3] and specific heat [4, 5], as well as a latent heat. The AF structure

of FeRh has been studied by neutron diffraction and is known as G-type [6–8]: the Fe site moments have FM coupling in (1 1 1) planes and AF coupling between the planes. The crystallographic direction of the moments themselves has not been reported. AF materials are important for memory technology, due to the exchange bias phenomenon [9], where their magnetic domain structure is particularly important but difficult to directly measure. The uniqueness of the AF–FM phase transition in FeRh and its temperature (just above room temperature) makes FeRh of current interest, in particular in thin-film form, where it has been proposed for use in

heat-assisted magnetic recording (HAMR) with an exchanged-coupled FM layer [10–12]. In this usage, FeRh is AF at the magnetic storage temperature (300 K), where it acts to stabilize the exchange-coupled FM layer, but FM at the writing temperature (400 K) where it helps with the writing process. In considering this process, information about the magnetic domain structure of both the FM and the AF phase is useful.

A first-order transition proceeds by nucleation and growth of a new distinct phase out of the original phase. Several recent studies have aimed at characterizing the nucleation and growth process [13, 14]. In particular, our group recently reported the direct observation of the temperature-driven nucleation and growth of the FM phase in epitaxial FeRh thin films using photoemission electron microscopy (PEEM) by x-ray magnetic circular dichroism (XMCD) at the Fe L_3 edge [15]. We showed that the evolution of the FM phase on both heating and cooling followed the expected transition as measured by magnetometry, and that the different stages of nucleation, growth and coalescence of the FM phase on heating could be identified, as well as other local details of the transition using this microscopic probe. The increasing use of PEEM to study FeRh is seen in recent publications [16–18]. XMCD is sensitive to the average magnetization $< M >$ and is therefore not sensitive to AF order which has no net magnetization. The vanishing XMCD signal on cooling indicated formation of the AF phase in well defined regions of the sample, but the AF phase itself could not be imaged. Therefore, characterization of the AF phase such as domain structure was not possible in this previous study.

Although an AF domain has no net magnetization, each antiparallel sublattice carries a magnetization M. X-ray magnetic linear dichroism (XMLD) is sensitive to $< M^2 >$ and can therefore probe the magnetic domain structure of both ferromagnets and antiferromagnets. While several studies have been successful at studying the microscopic structure of AF thin films in exchange-biased systems using XMLD, they have been limited to oxide compounds such as NiO, Fe_2O_3 and $LaFeO_3$ [19–21]. The challenge with using XMLD is that it probes the anisotropy of the electronic structure that is induced by axial spin alignment from the magnetic order (FM or AF). This results in changes in the fine structure of the x-ray spectrum which require a good energy resolution to be distinguished. Moreover, while for oxides the XMLD can be as large as 40% of the absorption signal, the reduced crystal-field splitting of electronic states in metals is thought to reduce this effect for metallic systems [22]. Several studies have reported successful experimental XMLD on FM magnetic transition metals (Fe, Co and Ni) in their metallic state as a way to probe the magnetocrystalline anisotropy, with maximum relative difference in absorption between the two linear polarizations ranging from 6 to 11% for Fe [23–25]. Several studies have also reported on the XMLD microscopy of metallic FM domains [26, 27] but few studies have attempted direct imaging of AF domains in a metallic sample such as FeRh. An additional reason is that metallic simple AF are not common: the well-known metallic AF (Cr, FeMn) have spin-wave or non-collinear structures which do not generate any XMLD signal.

In this work, we use both XMCD and XMLD in photoemission electron microscopy (PEEM) combined with image processing techniques to study the characteristics of the AF phase and its evolution with temperature upon cooling across the FM–AF transition in an epitaxial FeRh thin film. The goal of this work is twofold: to determine the domain structure of the AF phase in its stable state below the transition and to study its evolution out of the FM state in comparison to the evolution of the FM phase out of the AF phase, so as to obtain a complete picture of the nucleation and growth mechanisms involved in both parts of this transition.

2. Experimental techniques

Two sets of samples were grown. One set of FeRh films were grown for preliminary XLD experiments to ascertain feasability. These films were grown by magnetron sputtering from an equiatomic FeRh target onto different substrates: (0 0 1) MgO, c-plane sapphire and ion-beam-assist-deposited (IBAD) MgO, and capped with MgO. Details about the films characterization as well as the IBAD MgO substrate can be found in references [28–30]. The other sample used for the full XMLD and XMCD microscopy study is a 100 nm thick (0 0 1) FeRh thin film grown by magnetron sputtering from an FeRh alloy target onto (0 0 1) MgO substrate. Details of this sample synthesis and characterization can be found in reference [15]. The film was left uncapped since several capping materials have been shown to modify the magnetic properties near the top interface, as recently discussed in [31] and XMCD and XMLD-PEEM is extremely surface sensitive. To limit the formation of the native oxide layer, the sample was fabricated in our laboratory and then introduced in the PEEM microscope high vacuum chamber within 4 h. X-ray absorption spectroscopy (XAS) was recorded in the PEEM microscope chamber at room temperature before imaging and showed no significant oxidation of Fe.

The magnetic phase transition was verified by SQUID magnetometry. Figure 1 shows the temperature dependence of the magnetization of the uncapped sample in an applied field of 3 T (a large field is used to shift the transition below 400 K, the maximum temperature of the SQUID magnetometer). The middle of the transition upon cooling occurs at 349.5 K in 3 T, with a width of 25 K between the beginning and the end of the transition (bottom axis). By correcting for the temperature shift due to the field ($dT/dH = -8 \, K \, T^{-1}$) the transition from FM to AF is expected to occur between 388 K and 363 K in zero applied magnetic field (top axis). Images were taken as a function of temperature between 394 K (no AF phase) and 360 K (fully AF according to magnetometry), with additional imaging in the fully AF phase at 300 K.

PEEM imaging was performed at ALS PEEM Beamline 11.0.1 [32] at the Fe L_3 edge, using low-energy secondary electrons with a spatial resolution of 30 nm. Magnetic contrast is obtained by using either left and right circularly or parallel p and perpendicular s linearly polarized x-rays in XMCD and XMLD respectively.

To produce XMLD images, PEEM images were recorded at energies $E_1 = 706.7 \, eV$ and $E_2 = 707.7 \, eV$ near the Fe L_3
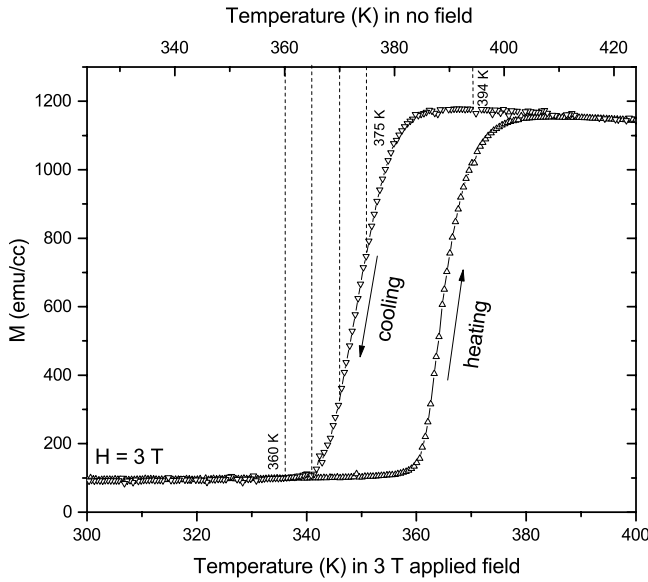
Figure 1. Magnetic characterization of the FeRh thin film. The magnetization as a function of temperature was measured in 3 T (bottom axis). The vertical dashed lines show the temperature at which the PEEM images were recorded upon cooling in no external field (top axis): 394 K (fully FM), 375 K, 370 K, 365 K (mixed FM and AF) and 360 K (fully AF).

edge and with orthogonal polarization directions p, s. These energies correspond to a positive maximum at the L_3 peak and a negative minimum about 1 eV below, therefore giving a maximum XMLD signal. Images are computed by taking the ratio with the two energies and the ratio with the two polarizations:

$$I_{XMLD} = \frac{p(E_1)/s(E_1)}{p(E_2)/s(E_2)} \qquad (1)$$

This double division improves the XMLD contrast (close to the limit of the instrument of 0.2%) by better normalization of topographic and chemical features.

XMCD images are generated by the ratio at a single energy:

$$I_{XMCD} = \frac{I_+(E_1)}{I_-(E_1)} \qquad (2)$$

To improve the signal-to-noise ratio of the images, a large number of snapshots were recorded and then averaged, typically 100–200 snapshots for XMLD images and 10–20 snapshots for XMCD images. The XMCD contrast is quite strong and does not require the same statistics to produce good quality images.

The temperature of the sample was controlled by a custom stage with a ceramic heater with low magnetic stray field for heating power, a cryogenic cold source for controlled cooling power, and a silicon diode thermometer for temperature reading. The temperature of the sample was stabilized for each measurement and kept constant for the duration of recording of the several snapshots required for each image (time ranging from a few minutes to about an hour).

In order to determine the representative domain size of the FM and AF phases, the characteristic length of the XMCD and XMLD-PEEM images is obtained by autocorrelation analysis.

The autocorrelation of a function is the cross-correlation with itself as defined by

$$\Phi_{f,f}(x, y) = f(x, y) * f(x, y)$$
$$= \int \int f(\xi - x, \eta - y) f(x, y) d\xi d\eta \qquad (3)$$

and is numerically computed using the following:

$$\Phi_{f,f}(x, y) = F^{-1}[F(u, v)F^*(u, v)] \qquad (4)$$

with $F(u, v)$ the Fourier transform of $f(x, y)$ calculated in MATLAB by Fast Fourier Transform (FFT). The origin of the autocorrelation image $\Phi_{f,f}(0, 0)$, located at the center of the image, is a global maximum of the autocorrelation function. For the images analyzed here, the amplitude of the autocorrelation function decreases sharply with increasing x and y. The autocorrelation images are found to be mostly radially symmetric (the only exception is the XMCD image of the fully FM phase), indicating that the average size of the features is isotropic with x and y; therefore, a radial average of the autocorrelation is calculated and plotted as a function of radial pixel. To extract a correlation length that is representative of the actual length scale of the image features, contributions from the instrument (short-range contribution) and background are accounted for. The image background can result in a long-range contribution (e.g. uneven image background) with a broad peak. This contribution is removed by fitting a 2-dimensional linear plane to the image surface and subtracting that plane. The uneven background is due to the non-constant profile of the x-ray beam. The instrument contribution is due to the detector and microscope point spread functions which result in a sharp autocorrelation feature near zero. It is determined experimentally by a fitting procedure. The radial profile is fitted with a combination of two Gaussian distributions $a \exp(-(x/b)^2)$. The short-range Gaussian distribution is due to the instrument and determined to be 48 nm, corresponding to a spread of 5 pixels. The instrument point spread function is independent of temperature. The correlation length of the image is defined as twice the Gaussian fit parameter b of the long-range Gaussian distribution. This standard autocorrelation method is used for example to analyze chemical heterogeneity in scanning tunnelling microscope images, grain size distributions in geology and fluorophore distributions in biology [33–35]. Note that this correlation length referred to in this work is the characteristic length of the image (expected to be related to magnetic domain effects), not the spin-correlation length related to the magnetic order.

A similar method can also be applied to determine if two different images (e.g. XMCD and XMLD images at the same temperature or XMLD images at different temperatures) are correlated. The cross-correlation

$$\Phi_{f,g}(x, y) = f(x, y) * g(x, y) \qquad (5)$$

is computed instead, and the same treatment is applied. If there is long-range correlation between f and g, the origin $\Phi_{f,g}(0, 0)$ is a maximum.

The robustness and consistency of the autocorrelation is tested by computing the autocorrelation with different window
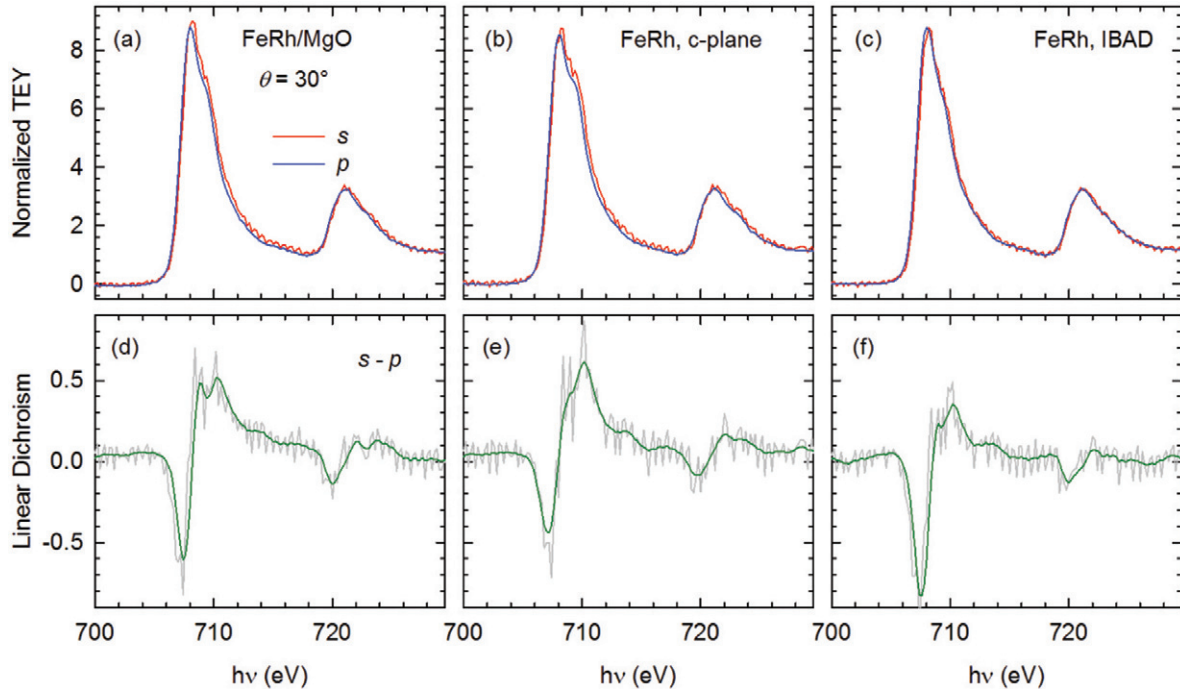
Figure 2. XLD spectrum recorded at room temperature (AF phase) in total electron yield mode on an FeRh film capped with MgO deposited on (*a*) MgO substrate, (*b*) c-plane sapphire substrate, and (*c*) IBAD MgO. The upper panels show the two spectra recorded with *s* and *p* polarizations and the lower panels show the difference *s* − *p* and the presence of a maximum and a minimum near the Fe L_3 edge. Raw data is shown in light grey. Smoothing was applied to remove instrument noise and is shown overlaid.

sizes (ranging from 512 by 512 to 900 by 900 pixels), and error bars in correlation length are extracted from the standard deviation of the fits produced with different window size. Note that the full field of view size is 1030 by 1050 pixels. Note that the error bars correspond to a correlation length fit confidence value and do not account for all errors.

3. Spatially averaged spectroscopy results

Spatially averaged Fe $L_{2,3}$ x-ray absorption (XAS) and linear dichroism (XLD) spectra were measured via total electron yield (TEY) on several MgO-capped FeRh films grown on different substrates to confirm the existence of XLD. The FeRh films, nominally 150 nm thick, were grown on MgO (0 0 1), c-plane sapphire, and (0 0 1) IBAD MgO [29] substrates and capped with 3 nm MgO. TEY measurements in figure 2 used the same undulator and monochromator that illuminated the PEEM chamber but on a separate branchline. Linearly polarized x-rays 30 degrees from grazing incidence illuminated the samples with *s* and *p*-polarization probing absorption in and mostly out of the film plane, respectively. XAS spectra in figures 2(*a*)–(*c*) were analyzed by subtracting extrapolated pre-edge intensity and normalizing the remainder to 1 above the L_2 line. With samples at room temperature, the *s* − *p* XLD in figures 2(*d*)–(*f*) should sense magnetic linear dichroism (XMLD) from the AF FeRh [36]. Metallic FM Fe [23–25, 37] and AF FeRh [36] exhibit XMLD having a characteristic dipolar shape at the L_3 and L_2 edges consistent with that observed in these capped FeRh samples.

However, the XAS and XLD in figure 2 reveal sensitivity to oxidized Fe at the MgO/FeRh interface as well as to unoxidized Fe within the FeRh layer. The presence of oxidized Fe is revealed by a distinct shoulder on the high energy side of the L_3 peaks, and a less distinct shoulder at the L_2 peaks. This is evident from the comparison of XAS spectra from the MgO-capped samples with a freshly grown, uncapped FeRh sample measured in the PEEM chamber as in figure 3. The uncapped sample shares the sharp L_3 peak at low energy and lacks the oxide shoulder. For PEEM measurements we investigate the uncapped sample whose XAS spectra reveal no indication of oxidation in comparison to the MgO-capped samples.

It is expected that some Fe oxidation will occur at the MgO/FeRh interface given the comparable enthalpy of formation of iron oxides and MgO. The oxide shoulders of the Fe XAS spectra are not consistent with well-defined, ordered Fe-oxides [38], however, although their position is indicative of some degree of Fe oxidation. This points to the high sensitivity of the magnetization in the surface region of FeRh due to chemical perturbations induced for example by capping materials [31].

Understanding that the XAS of the capped samples contains signatures from both oxidized and unoxidized Fe allows us to interpret the XLD spectra in figures 2(*d*)–(*f*) as having two contributions, one from the oxidized interfacial region, and one from the interior, unoxidized FeRh film. The negative XLD L_3 peak is on the rising edge of the unoxidized Fe line, consistent with the dipolar XMLD from Fe [23–25, 37] and FeRh [36], and is where PEEM images were collected. The positive XLD features on the high side of the L_3 line are split into 2 peaks, and the higher energy feature may be associated with the oxidized Fe near the cap layer. Interestingly, both the XAS and XLD of the capped samples indicate that the extent
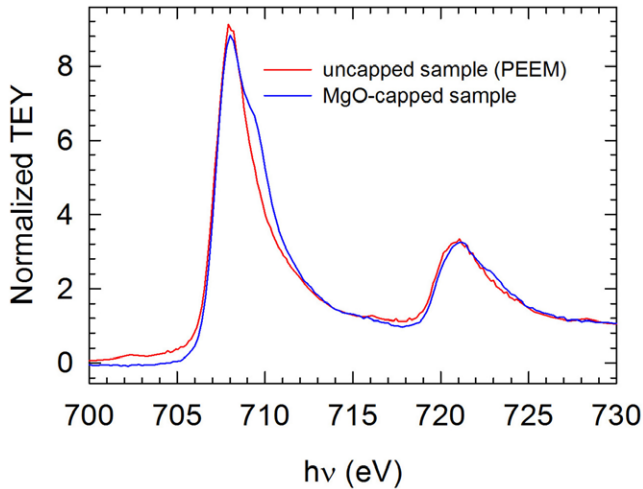
Figure 3. Comparison of XAS spectra from the MgO-capped samples with a freshly grown, uncapped FeRh sample measured in the PEEM chamber.

of oxidation may depend on substrate, presumably through differences in microstructure of the FeRh films. Different substrates induce different crystallographic orientation and strain state: FeRh on MgO has [0 0 1] out-of-plane orientation and is cubic, FeRh on c-plane sapphire has [1 1 1] out-of-plane orientation and FeRh on IBAD MgO has [0 0 1] out-of-plane orientation with a tetragonal distortion [29, 30]. The negative XLD L_3 feature is seen on all three samples with different orientation and strain state. This is a strong indication that at least part of the signal is independent from structural distortion of the AF phase.

4. Microscopy results

While TEY-XAS of MgO-capped films showed contribution to XLD from oxidized and unoxidized Fe, PEEM microscopy was performed on an uncapped film which showed no evidence of surface oxidation in XAS. We now turn to the use of PEEM microscopy to image the uncapped FeRh thin film and the evolution of the XMCD and XLD patterns with temperature. Figure 4 shows a summary of the XMCD images recorded at different temperatures across the cooling transition from FM to AF, starting at 394 K in the fully FM phase and cooling to 360 K at an almost completed transition with only few residual FM nuclei left (figures 4(a)–(e)), and the XLD images recorded at the same temperatures (figures 4(f)–(j)). With the XMCD images, we observe the progressive disappearance of the FM phase upon cooling: first a reduction in the size of the domains, then in the number of the FM domains, in full agreement with our previous XMCD-PEEM observation reported in [15].

The XMCD image figure 4(e) at 360 K shows that the surface is mostly AF. In the corresponding XLD image figure 4(j) small features with a weak but noticeable XLD contrast are observed. We consider the possibility of the weak XLD contrast coming from residual topographic features that did not get entirely removed in the image computation. Visual comparison to the topography of the sample shows no clear similarity between the two, indicating that the image

computation correctly removes non-XLD features. Another possible cause of linear dichroism is a parasitic moment, e.g. AF moments which are not completely collinear and result in some net uncompensated moment. Such parasitic moment would result in an XMCD pattern which matches the XLD pattern. However no such XMCD pattern is detected at 360 K. The possibility of a surface FM state as the origin of the XLD image is excluded by the absence of contrast in the XMCD image. Finally, we consider the possibility for the XLD signal to originate from an AF surface layer different from the bulk of the film. The most likely candidate material is an Fe oxide. This is ruled out since there is no evidence of surface oxidation in XAS. We can therefore conclude that these XLD contrast features originate from AF FeRh and that the changes in PEEM images with temperature reflect the changes in the AF domain pattern in the FeRh film.

Figures 4(a) and (f) show the fully FM phase in XMCD and XLD. An XLD pattern with strong contrast is clearly visible, due entirely to the FM phase (as previously discussed, XLD includes contributions from both AF and FM phases). Figures 5(a) and (b) show the same XMCD and XLD images with constant intensity contours computed at the image mean intensity value overlaid on each dichroic image. Comparison of the two patterns is then done by overlaying both contour patterns in figure 5(c). An excellent match is observed between the two patterns thus establishing spatial correlation between the two. This clearly shows that a spatially resolved XLD signal is detected from the FeRh FM phase.

We further confirmed that the high temperature XLD contrast is magnetic in origin by heating a similar sample above its Curie temperature $T_C = 573$ K [39]. Both XMCD and XLD contrasts disappear above T_C which supports that both contrasts are due to the FM phase. The FM origin of the XLD contrast in the FM phase is also strong evidence of the magnetic origin of the XLD contrast in the AF phase as well. Since the magnitude of the Fe moments in the FM and AF phases are similar with 3.2 and 3.1 μ_B respectively [30] and the mechanism for XMLD contrast is independent of the AF or FM order, our measurement should be capable of detecting magnetic contrast from the AF phase. Therefore, we attribute the image contrast to x-ray magnetic linear dichroism and use it to study the magnetic structure of the AF phase. We will now refer to XMLD in the remainder of the paper.

The XMLD image at 394 K shows the FM domain structure, and those taken at 375 K and below show a structure finer than the FM structure with no change evident to the eye from 370 to 360 K.

5. Discussion

In the FM to AF transition upon cooling, figures 4(a)–(c) show a reduction in the size of the FM domains. A quantitative analysis is done using the image correlation length method described in the experimental techniques section. Figure 6(a) shows the average radial profile of the autocorrelation of the XMCD images at all 5 temperatures. The x axis has been converted from pixel to nm based on the magnification of the microscope used (10 μm for 1000 pixels). The steepness of the
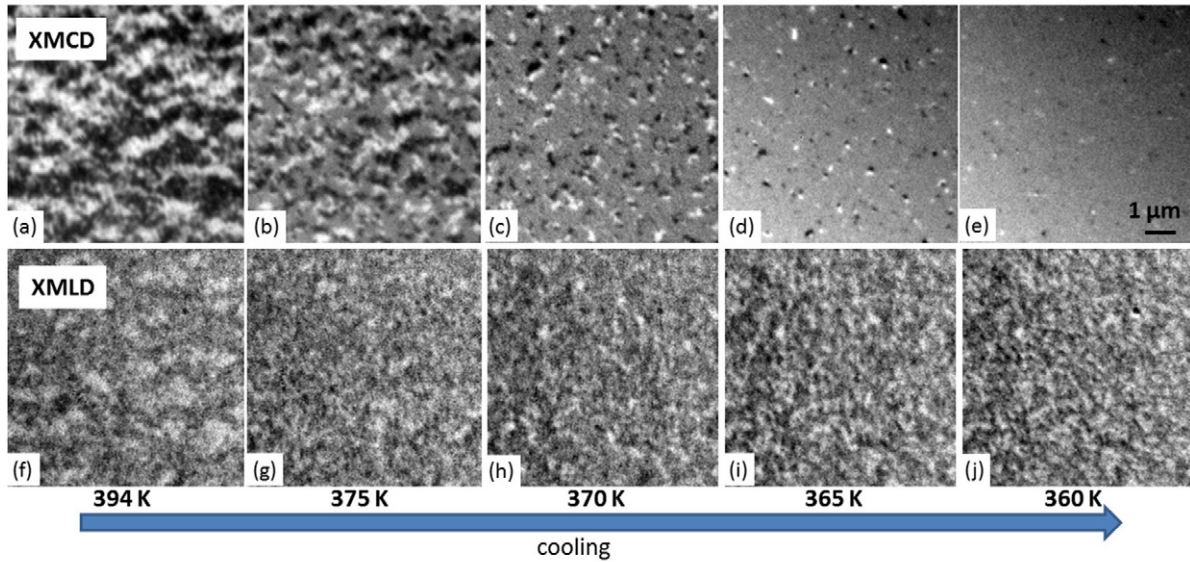
Figure 4. Comparison of (*a*)–(*e*) XMCD and (*f*)–(*j*) XMLD-PEEM images recorded upon cooling of FeRh thin film from 395 K (fully FM) to 360 K (mostly AF). Several intermediate mixed phase state are shown at 375 K, 370 K and 365 K. Each XMLD-PEEM image is obtained by averaging 60 snapshots taken at two different energies ($E_1 = 706.7$ eV, $E_2 = 707.7$ eV) and two different polarizations (parallel *p* and perpendicular *s*) (240 snapshots total) and computing $(p(E_1)/s(E_1))/(p(E_2)/s(E_2))$ so as to maximize the XMLD contrast. Each XMCD-PEEM image is obtained by averaging 6 snapshots taken at the Fe L_3 edge for opposite circular polarization (12 snapshots total) and dividing them (approximation of asymmetry).
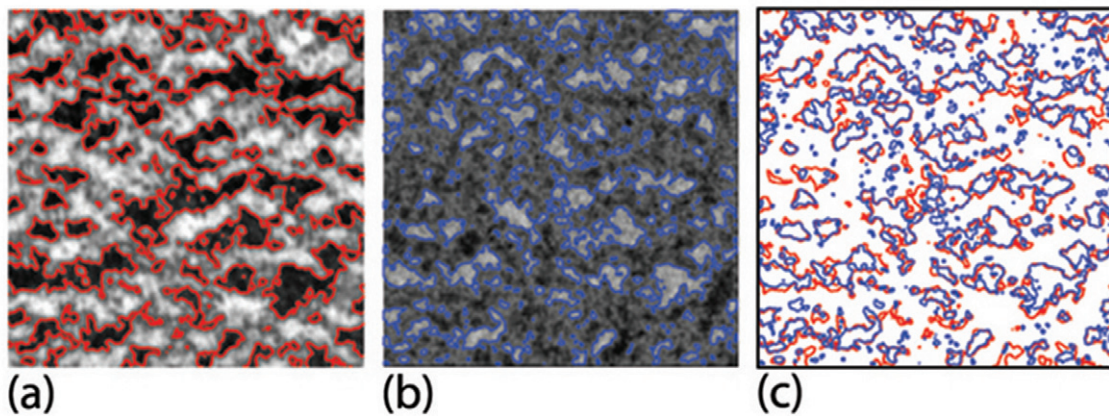

Figure 5. Comparison of domain pattern in XMCD-PEEM image to XMLD-PEEM features in the fully FM phase at 394 K. Contours of constant intensity are drawn to make the FM domains apparent in (*a*) the XMCD image and (*b*) the corresponding XMLD pattern in the XMLD image recorded at the same temperature. (*c*) Overlay of the two contour images showing the good spatial correlation between the two signals.

autocorrelation profile increases with decreasing temperature, indicating a decrease in the correlation length. The first 3 temperature steps (394 K to 370 K) show a single smooth decaying curve while the 365 K and 360 K curves become sharper and have a kink, especially visible at 360 K. The appearance of the kink is due to the increase in relative magnitude of the contribution from the instrument resulting in a sharp Gaussian with small correlation length near the origin. Above 370 K, the number of pixels that carry a FM signal is large compared to the non-magnetic background. Below 365 K, FM pixels are a minority compared to the background, and the contribution from the instrument is dominant in the autocorrelation.

In the autocorrelation profiles of XMCD images ranging from 394 K to 370 K, the relative contribution from the instrument is negligible, and a single broad Gaussian fit works well. The strong contribution from the instrument point spread function appears in the autocorrelation profiles at 365 K and 360 K in figure 6. The two-Gaussian fit is shown in figures 6(*a*), insets (*b*) and (*c*). Next we look at the relative magnitude of the instrument Gaussian compared to the second Gaussian. Both Gaussians are plotted in figures 6 insets (*b*) and (*c*). The relative magnitude of the two Gaussians with each other is evidenced. While at 365 K the instrument Gaussian is lower than the second Gaussian, the opposite is seen at 360 K. This indicates that at 360 K, the correlation length analysis is not meaningful
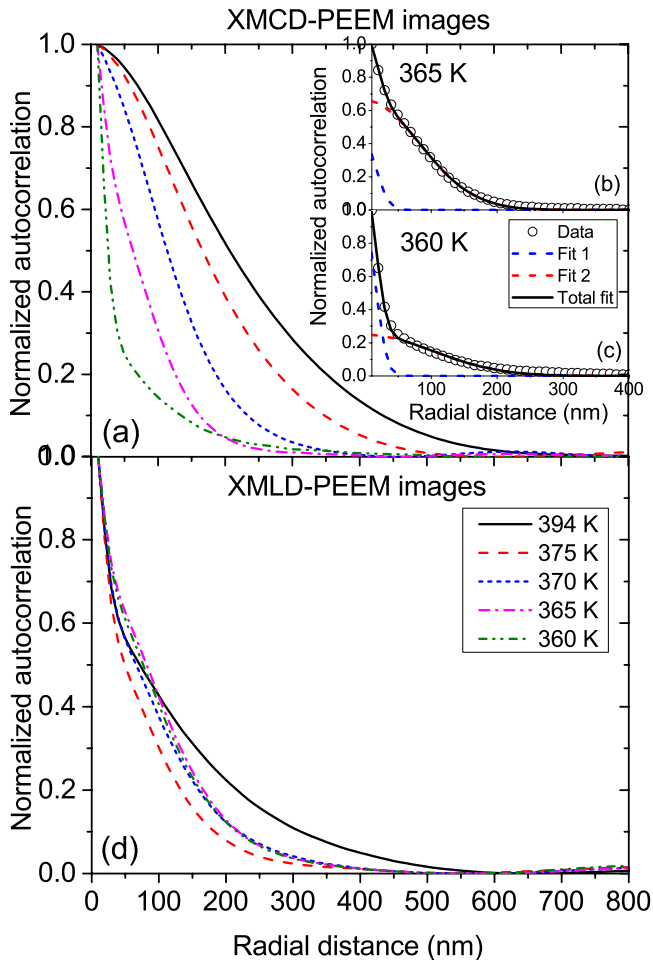
Figure 6. (*a*) Normalized autocorrelation profile (radially averaged) for XMCD images at 394 K, 375 K, 370 K, 365 K and 360 K. Note that the magnitude of the autocorrelation signal decreases as the temperature decreases (due to decrease in number of pixels that carry a FM signal), but we choose to show here the normalized signal to emphasize the change in correlation length. Insets: Double Gaussian fits of autocorrelation radial profiles at (*b*) 365 K and (*c*) 360 K. In each inset, each separate Gaussian is shown as well as the total fit of the sum of both Gaussians. (*d*) Normalized autocorrelation profile (radially averaged) for XMLD images at 394 K, 375 K, 370 K, 365 K and 360 K.

due to the small number of pixels with FM contrast. The low-amplitude broad residual contribution to the autocorrelation is attributed to error from an imperfect background subtraction. At 365 K and above, the characteristic length is calculated from the second broader Gaussian.

We now compute the normalized autocorrelation radial profiles of the XMLD images from figure 4. In figure 6(*d*) we notice that the autocorrelation radial functions of the XMLD images from 375 K to 360 K show a strong relative contribution of the instrument. This suggests that the autocorrelation analysis will reach its limit on the XMLD images as it did for the XMCD image at 360 K.

For XMCD images above 370 K, the correlation length ranges from 554 ± 15 nm at 394 K to 323 ± 10 nm at 370 K. Figure 7 shows that the correlation length is a good quantitative measure of the average FM domain size. Circles of diameter equal to the correlation length are overlaid on the XMCD
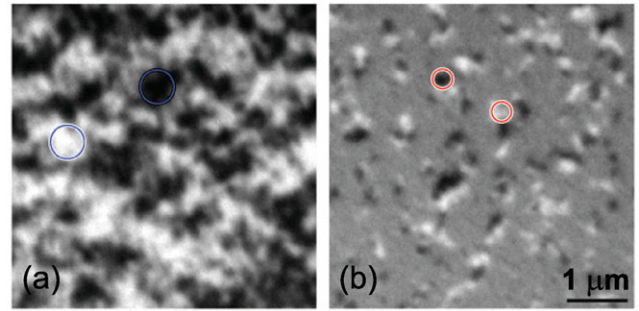

Figure 7. Comparison of the correlation length as calculated by the Gaussian fit parameter in the autocorrelation method to the directly observed FM domain size at (*a*) 394 K where two blue circles of diameter 554 nm are shown near two FM domains (one black, one white) and (*b*) 370 K where two red circles of diameter 323 nm are shown near two regions still FM at 370 K.

images taken at 394 K (figure 7(*a*)) and 370 K (figure 7(*b*)) and show a good agreement with the size of the domains observed at each temperature. The FM domains at 370 K are smaller in size because the FM phase coexists with the AF phase, so only finite regions of the film are FM as opposed to the entire field of view at 394 K.

Analysis of the 394 K XMLD image gives a correlation length of 457 ± 10 nm. This is ∼100 nm lower than the correlation length of the XMCD image at the same temperature. We attribute the discrepancy to the lower magnitude of the XMLD signal compared to the XMCD signal. Indeed while the XMCD autocorrelation is dominated by the magnetic signal, almost half of the XMLD autocorrelation amplitude is due to the instrument spread. This is consistent with the XMLD signal having a lower contrast to noise ratio than the XMCD signal.

The change in correlation length with temperature as calculated for each XMCD image and each XMLD image is shown in figure 8. The XMCD correlation length, a good measure of the average FM domain size, decreases gradually upon cooling, following the decrease in size of FM regions. The XMLD correlation length starts near the XMCD at 394 K in the FM phase, consistent with the fact that both XMCD and XMLD images resolve the FM structure in the fully FM phase. It then follows a sharp decrease to 279 nm at 375 K, outside the typical error bars of 10 nm, before increasing slightly above 300 nm and remaining mostly constant upon subsequent cooling. Note that 300 nm is much larger than the spatial resolution limit of the microscope, since FM nuclei as small as 60 nm are resolved in XMCD images.

The near absence of change in the evolution of the XMLD images' morphology and their correlation length upon cooling below 370 K can be due to two possible reasons: (1) individual AF domains are not resolved (e.g. below spatial resolution of 30–60 nm), and the correlation length is associated with larger scale groups of domains, (2) the AF domains experience little or no growth below 370 K. An AF phase transformation limited by nucleation is consistent with the knowledge that AF domains are typically associated with crystallographic defects; therefore, their size is limited by the size of defect-free regions in the FeRh thin film. Both explanations therefore point to a
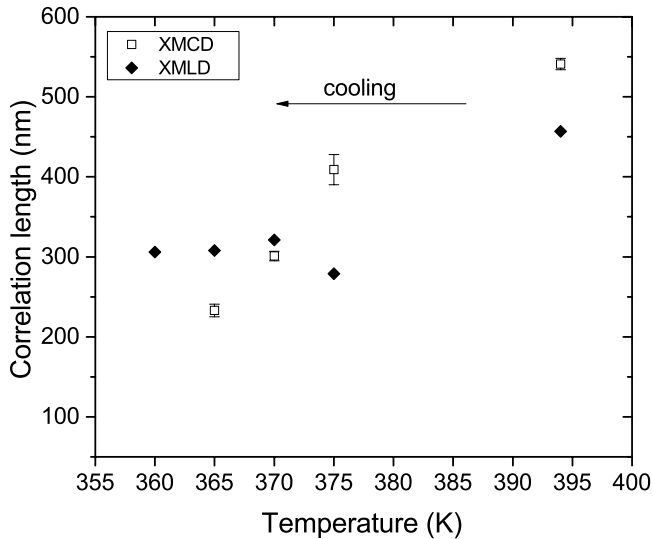
Figure 8. Evolution of the correlation length of XMCD and XMLD images with temperature. The correlation length is equal to twice the Gaussian fit parameter (of the broader Gaussian when two Gaussians are used). A single Gaussian fit was used for XMCD autocorrelations at 394 K, 375 K and 370 K and a double Gaussian fit was used for XMCD autocorrelation at 365 K, and for all XMLD autocorrelations.

small AF domain size (300 nm or less) limited by defects. The structural coherence length determined by Scherrer's formula on an out-of-plane 001 peak for FeRh thin films of similar quality to this one is 33 nm, significantly smaller than the 100 nm film thickness, therefore limited by structural defects such as point defects, low angle grain boundaries or chemical antiphase boundaries in this epitaxial film. We have no information on the in-plane structural coherence length, but it is unlikely to be significantly different than the out of plane. The 300 nm in-plane XMLD correlation length is large, an order of magnitude greater than the structural coherence length, suggesting that the magnetic coherence extends across the defects which limit the structural coherence. The features actually appear smaller to the eye in the images, but due to the high noise level, their size is difficult to measure. The larger correlation length could also be due to a domain morphology that is not granular (e.g. meandering domains) [40].

We acknowledge that the correlation length analysis might be at the limit of its validity for the XMLD images. To show that the AF features are nevertheless spatially resolved in the XMLD images, we turn to a cross-correlation analysis of XMLD images at different temperatures as a way to evidence a progressive evolution of features in the images. Two cross-correlation images are shown in figure 9 with the autocorrelation of the 365 K image for comparison. The correlation window size is 900 × 900 pixels, and images are displayed using the same colorscale (arbitrary units). Cross-correlations between XMLD image at a given temperature step and the temperature step immediately preceding and following have a global maximum at the origin. This means that the two successive images are spatially correlated and that many of the features are the same between the two images.

To further look at the nucleation of AF domains, we repeated the imaging of AF and FM phases in the same region

of the sample upon a second cooling cycle. In the case of heterogeneous nucleation, nucleation starts preferentially at defect sites. Although we do not spatially resolve the defects here, by comparing the nucleation sites between two different cooling cycles, we can determine to what extent they affect the transition. After a full transition upon cooling was recorded from 394 K to 360 K as shown in figure 4, the sample was heated back to 394 K, and the same temperature steps were recorded during the second cooling. Figure 10 shows the identical region of the sample in the fully FM phase (XMCD images (*a*) and (*b*)) before the first and second coolings, and in the mostly AF phase (XMLD images (*d*) and (*e*)) after the first and second coolings. The cross-correlation of the two XMCD images, shown in figure 10(*c*), allows us to determine how similar the first and second FM domain patterns are, which is otherwise difficult to evaluate visually. The absence of global maximum at the center of the image indicates that no long-range correlation exists between the first and second FM patterns. In contrast, the same cross-correlation evaluation of the two XMLD images, shown in figure 10(*f*), finds a global maximum at the center which means that the two images are strongly spatially correlated. Note that in [15] we showed that the nucleation of FM domains upon heating is heterogeneous, with a spread in nucleation temperature and a correspondence between the initial nucleation sites upon heating and the last remaining FM regions upon cooling. While nucleation of the FM phase is heterogeneous it is then followed by significant growth of the domains resulting in a non-reproducible final domain structure between repeated heating cycles, likely because the domains are large compared to the initial nuclei and their growth is less tightly linked to defects than their nucleation.

The observation of spatial correlation between the AF structures obtained in two separate cooling cycles is consistent with our interpretation that the AF domains are influenced by crystallographic defects. Even though the initial FM matrix is different between the two cooling steps, the final AF structure obtained is similar. This structure is not random. We suggest that the AF domains are pinned by the FeRh thin film defects which are stable through this temperature range, including the transition.

6. Summary

In summary, XMLD-PEEM was used to spatially resolve the AF and FM phases in an FeRh thin film. We established the magnetic origin of the XMLD features in the FM phase, and by comparison of FeRh XLD spectra with known XMLD spectra, showed that XMLD in the AF phase was also of magnetic origin. Autocorrelation analysis was used to determine the characteristic length of the magnetic features in the XMCD and XMLD images. While in the XMCD images the correlation length proved to be a good measure of the average FM domain size, the effectiveness of this analysis was limited for the XMLD images. A correlation length of ∼300 nm was computed for the AF phase. This value likely corresponds to groups of several AF domains, instead of single domains, and points to an AF domain size limited by defects. By studying the
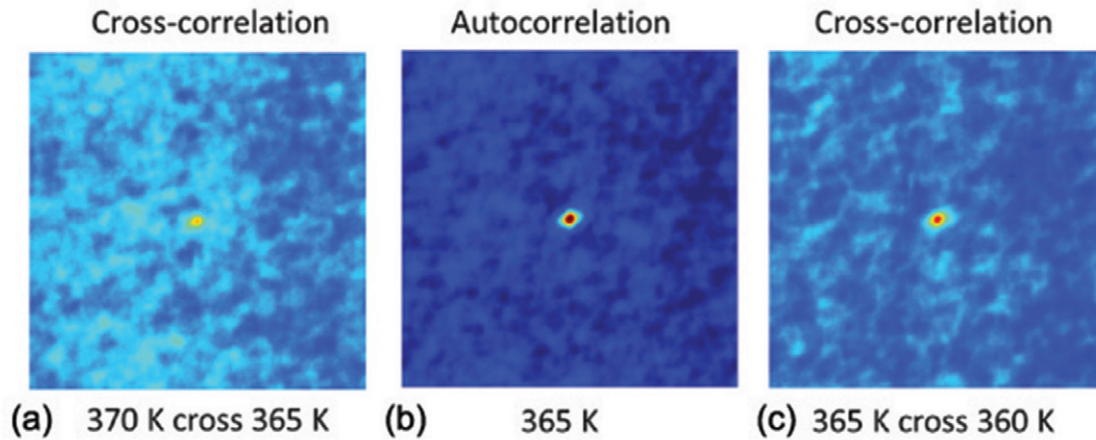
Figure 9. Cross-correlation of XMLD images at different temperatures: (*a*) between 370 K and 365 K images, (*b*) between 365 K image and itself (autocorrelation) and (*c*) between 365 K and 360 K images. Care was taken to compute the cross-correlation of the exact same region of the sample.
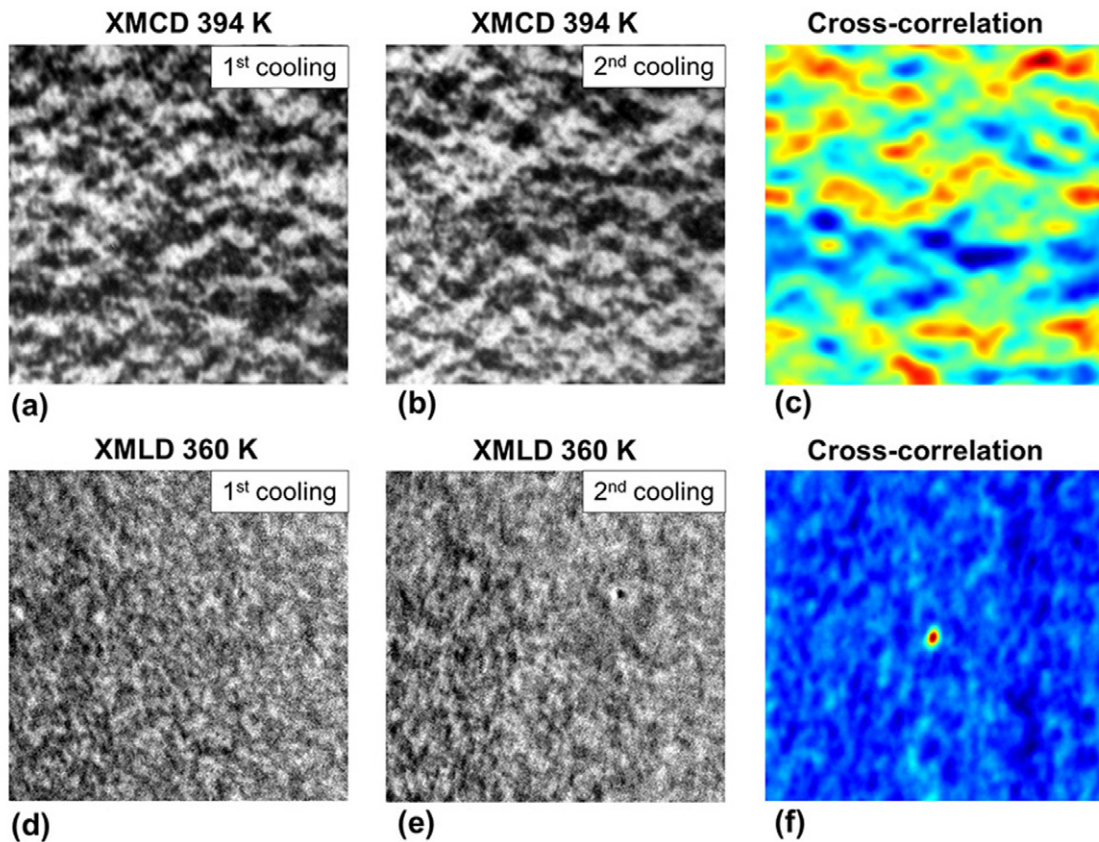

Figure 10. Comparison of XMCD and XMLD images recorded at the same temperature during 2 successive cooling cycles (field of view is 10 μm). XMCD images at 394 K in the fully FM phase before (*a*) the first cooling cycle, (*b*) the second cooling cycle, and their cross-correlation image (*c*). XMLD images at 360 K (mostly AF phase) at the end of (*d*) the first cooling cycle, (*e*) the second cooling cycle, and their cross-correlation image (*f*).

cross-correlation of successive XMLD images, we evidenced small local changes in the AF morphology upon cooling, further confirming the spatial resolution of the AF phase. Finally, we found that a non-random similar AF structure is reproduced by repeating the cooling transition, confirming that the AF domains are correlated to defects. We hope that this work will be useful for continued microscopic studies of the FeRh AF phase as well as other metallic AFs.

Acknowledgments

References

[1] Fallot M and Hocart R 1939 Sur l'apparition du ferromagnétisme par élévation de température dans des alliages de fer et de rhodium *Rev. Sci.* **77** 498–500

[2] De Bergevin F and Muldawer L 1961 Etude cristallographique de certains alliages fer-rhodium *C. R. Acad. Sci.* **252** 1347–9

[3] Kouvel J S and Hartelius C C 1962 Anomalous magnetic moments and transformations in the ordered alloy FeRh *J. Appl. Phys.* **33** 1343–4

[4] Kouvel J S 1966 Unusual nature of the abrupt magnetic transition in FeRh and its pseudobinary variants *J. Appl. Phys.* **37** 1257–8

[5] Richardson M J, Melville D and Ricodeau J A 1973 Specific heat measurements on an Fe Rh alloy *Phys. Lett.* A **46** 153–4

[6] Shirane G, Nathans R and Chen C W 1964 Magnetic moments and unpaired spin densities in the Fe–Rh alloys *Phys. Rev.* **134** A1547–53

[7] Bertaut F, de Bergevin F and Roult G 1963 Etude par diffraction neutronique de $Fe_{0,47}Rh_{0,53}$ *C. R. Acad. Sci.* **256** 1688–91

[8] Wollan E O and Koehler W C 1955 Neutron diffraction study of the magnetic properties of the series of perovskite-type compounds $[(1 − x)La, xCa]Mno_3$ *Phys. Rev.* **100** 545–63

[9] Noguès J and Schuller I K 1999 Exchange bias *J. Magn. Magn. Mater.* **192** 203–32

[10] Nam N T, Lu W and Suzuki T 2009 Exchange bias of ferromagnetic/antiferromagnetic in FePt/FeRh bilayers *J. Appl. Phys.* **105** 07D708

[11] Thiele J-U, Maat S and Fullerton E E 2003 FeRh/FePt exchange spring films for thermally assisted magnetic recording media *Appl. Phys. Lett.* **82** 2859–61

[12] Kneller E F and Hawig R 1991 The exchange-spring magnet: a new material principle for permanent magnets *IEEE Trans. Magn.* **27** 3588–60

[13] Maat S, Thiele J-U and Fullerton E E 2005 Temperature and field hysteresis of the antiferromagnetic-to-ferromagnetic phase transition in epitaxial FeRh films *Phys. Rev.* B **72** 214432

[14] Manekar M, Mukherjee C and Roy S B 2007 Imaging of time evolution of the first-order magneto-structural transition in Fe–Rh alloy using magnetic force microscopy *Europhys. Lett.* **80** 17004

[15] Baldasseroni C, Bordel C, Gray A X, Kaiser A M, Kronast F, Herrero-Albillos J, Schneider C M, Fadley C S and Hellman F 2012 Temperature-driven nucleation of ferromagnetic domains in FeRh thin films *Appl. Phys. Lett.* **100** 262401

[16] Mariager S O, Le Guyader L, Buzzi M, Ingold G and Quitmann C 2013 Imaging the antiferromagnetic to ferromagnetic first order phase transition of FeRh arXiv e-prints arXiv:1301.4164

[17] Kinane C J *et al* 2014 Observation of a temperature dependent asymmetry in the domain structure of a pd-doped FeRh epilayer *New J. Phys.* **16** 113073

[18] de Vries M A, Loving M, McLaren M, Brydson R M D, Liu X, Langridge S, Lewis L H and Marrows C H 2014 Asymmetric melting and freezing kinetics of the magnetostructural phase transition in b2-ordered FeRh epilayers *Appl. Phys. Lett.* **104** 232407

[19] Scholl A *et al* 2000 Observation of antiferromagnetic domains in epitaxial thin films *Science* **287** 1014–6

[20] Nolting F *et al* 2000 Direct observation of the alignment of ferromagnetic spins by antiferromagnetic spins *Nature* **405** 767–9

[21] Kuiper P, Searle B G, Rudolf P, Tjeng L H and Chen C T 1993 X-ray magnetic dichroism of antiferromagnet Fe_2O_3: the orientation of magnetic moments observed by Fe 2*p* x-ray absorption spectroscopy *Phys. Rev. Lett.* **70** 1549–52

[22] Stöhr J and Siegmann H C 2006 *Magnetism, from Fundamentals to Nanoscale Dynamics* (*Springer Series in Solid-State Sciences*) (Berlin: Springer)

[23] Schwickert M M, Guo G Y, Tomaz M A, O'Brien W L and Harp G R 1998 X-ray magnetic linear dichroism in absorption at the *l* edge of metallic Co, Fe, Cr, and V *Phys. Rev.* B **58** R4289–92

[24] Dhesi S S, van der Laan G and Dudzik E 2002 Determining element-specific magnetocrystalline anisotropies using x-ray magnetic linear dichroism *Appl. Phys. Lett.* **80** 1613–5

[25] Kuneš J, Oppeneer P M, Valencia S, Abramsohn D, Mertins H-Ch, Gudat W, Hecker M and Schneider C M 2004 Understanding the XMLD and its magnetocrystalline anisotropy at the $l_{2,3}$-edges of 3d transition metals *J. Magn. Magn. Mater.* **272–6** 2146–7 (*Proc. of the Int. Conf. on Magnetism (ICM 2003)*)

[26] Finazzi M, Brambilla A, Biagioni P, Graf J, Gweon G-H, Scholl A, Lanzara A and Duò L 2006 Interface coupling transition in a thin epitaxial antiferromagnetic film interacting with a ferromagnetic substrate *Phys. Rev. Lett.* **97** 097202

[27] Kuch W, Offi F, Chelaru L I, Wang J, Fukumoto K, Kotsugi M, Kirschner J and Kuneš J 2007 Huge magnetocrystalline anisotropy of x-ray linear dichroism observed on CoFeMn bilayers *Phys. Rev.* B **75** 224406

[28] Cooke D W, Hellman F, Groves J R, Clemens B M, Moyerman S and Fullerton E E 2011 Calorimetry of epitaxial thin films *Rev. Sci. Instrum.* **82** 023908

[29] Cooke D W, Hellman F, Baldasseroni C, Bordel C, Moyerman S and Fullerton E E 2012 Thermodynamic measurements of Fe–Rh alloys *Phys. Rev. Lett.* **109** 255901

[30] Bordel C, Juraszek J, Cooke D W, Baldasseroni C, Mankovsky S, Minár J, Ebert H, Moyerman S, Fullerton E E and Hellman F 2012 Fe spin reorientation across the metamagnetic transition in strained FeRh thin films *Phys. Rev. Lett.* **109** 117201

[31] Baldasseroni C *et al* 2014 Effect of capping material on interfacial ferromagnetism in FeRh thin films *J. Appl. Phys.* **115** 043919

[32] Doran A, Church M, Miller T, Morrison G, Young A T and Scholl A 2012 Cryogenic {PEEM} at the advanced light source *J. Electron Spectrosc. Related Phenom.* **185** 340–46 (Photoelectron microscopy, Time resolved pump-probe {PES})

[33] McKay H A, Chen H, Feenstra R M and Poole P J 2003 Scanning tunneling microscopy images of III–V semiconductor alloys: strain effects *J. Vac. Sci. Technol.* **21** 18–22

[34] Rubin D M 2004 A simple autocorrelation algorithm for determining grain size from digital images of sediment *J. Sedimentary Res.* **74** 160–5

[35] Robertson C and George S C 2012 Theory and practical recommendations for autocorrelation-based image correlation spectroscopy *J. Biomed. Opt.* **17** 080801

[36] Marti X *et al* 2014 Room-temperature antiferromagnetic memory resistor *Nat. Mater.* **13** 367–74

[37] Kortright J B and Kim S-K 2000 Resonant magneto-optical properties of Fe near its 2*p* levels: measurement and applications *Phys. Rev.* B **62** 12216–28

[38] Miedema P S and de Groot F M F 2013 The iron l edges: Fe 2p x-ray absorption and electron energy loss spectroscopy *J. Electron Spectrosc. Related Phenom.* **187** 32–48

[39] Swartzendruber L J 1984 The FeRh (iron-rhodium) system *Bull. Alloy Phase Diagr.* **5** 456–62

[40] Hellman F, Shapiro A L, Abarra E N, Robinson R A, Hjelm R P, Seeger P A, Rhyne J J and Suzuki J I 1999 Long ferromagnetic correlation length in amorphous TbFe$_2$ *Phys. Rev. B* **59** 11408–15